Numerical Simulation of Cloud–Clear Air Interfacial Mixing: Effects on Cloud Microphysics

MIROSLAW ANDREJCZUK

Los Alamos National Laboratory, Los Alamos, New Mexico

WOJCIECH W. GRABOWSKI

National Center for Atmospheric Research, Boulder, Colorado

SZYMON P. MALINOWSKI

Institute of Geophysics, Warsaw University, Warsaw, Poland

PIOTR K. SMOLARKIEWICZ

National Center for Atmospheric Research, Boulder, Colorado

(Manuscript received 11 January 2006, in final form 22 March 2006)

ABSTRACT

This paper extends the previously published numerical study of Andrejczuk et al. on microscale cloud–clear air mixing. Herein, the primary interest is on microphysical transformations. First, a convergence study is performed—with well-resolved direct numerical simulation of the interfacial mixing in the limit—to optimize the design of a large series of simulations with varying physical parameters. The principal result is that all conclusions drawn from earlier low-resolution ($\Delta x = 10^{-2}$ m) simulations are corroborated by the high-resolution ($\Delta x = 0.25 \times 10^{-2}$ m) calculations, including the development of turbulent kinetic energy (TKE) and the evolution of microphysical properties. This justifies the use of low resolution in a large set of sensitivity simulations, where microphysical transformations are investigated in response to variations of the initial volume fraction of cloudy air, TKE input, liquid water mixing ratio in cloudy filaments, relative humidity (RH) of clear air, and size of cloud droplets. The simulations demonstrate that regardless of the initial conditions the evolutions of the number of cloud droplets and the mean volume radius follow a universal path dictated by the TKE input, RH of clear air filaments, and the mean size of cloud droplets. The resulting evolution path only weakly depends on the progress of the homogenization. This is an important conclusion because it implies that a relatively simple rule can be developed for representing the droplet-spectrum evolution in cloud models that apply parameterized microphysics. For the low-TKE input, when most of the TKE is generated by droplet evaporation during mixing and homogenization, an inhomogeneous scenario is observed with approximately equal changes in the dimensionless droplet number and mean volume radius cubed. Consistent with elementary scale analysis, higher-TKE inputs, higher RH of cloud-free filaments, and larger cloud droplets enhance the homogeneity of mixing. These results are discussed in the context of observations of entrainment and mixing in natural clouds.

1. Introduction

The impact of entrainment and cloud–clear air mixing on the spectra of cloud droplets is an important yet still unresolved issue in cloud physics. As far as bulk thermodynamical properties of clouds are concerned, elementary conservation principles of total water and moist static energy are sufficient to derive the temperature, water vapor, and cloud water of the homogenized mixture of cloudy and cloud-free air. Predicting the evolution of a cloud droplet spectrum, on the other hand, requires additional constraints because situations where cloud water after homogenization is distributed over either large number of small droplets or small

Corresponding author address: Dr. Miroslaw Andrejczuk, Los Alamos National Laboratory, MS D401, Los Alamos, NM 87545. E-mail: miroslaw@lanl.gov

number of large droplets are equally possible. The microscale processes—molecular diffusion of water vapor and heat, sedimentation of cloud droplets across the interface between saturated cloudy filaments and subsaturated clear air, and either complete or partial evaporation of droplets—determine the spectrum of cloud droplets after homogenization. In particular, the width of the droplet spectrum critically depends on whether the mixing is homogeneous (i.e., all droplets are exposed to the same subsaturation) or inhomogeneous (i.e., the degree of droplet evaporation varies). On larger scales, in turn, the spectral width is important for the water cycle because it determines the onset of gravitational coalescence in warm clouds (cf. Lasher-Trapp et al. 2005and references therein). Furthermore, transformation of cloud droplet spectrum due to entrainment and mixing is critical for radiative properties of stratocumulus (Chosson et al. 2004) and shallow convection (Grabowski 2006), cloud systems essential for the earth's climate. Herein, we investigate interactions between the cloud microphysical processes and turbulence with the emphasis on the net effect on the spectrum of cloud droplets.

This paper extends our earlier study (Andrejczuk et al. 2004, hereafter AGMS) that reported results from the pilot series of numerical simulations of microscale (submeter) turbulent mixing between cloudy and clear air. The AGMS simulations were motivated by the laboratory investigations of cloud–clear air interfacial mixing of Malinowski et al. (1998; see also Korczyk et al. 2006) and were aimed at bridging the gap between laboratory experiments and natural clouds. The AGMS simulations were set forth in an idealized scenario of decaying moist turbulence, augmenting a homogeneous isotropic turbulence study of Herring and Kerr (1993). To assess the role of larger-scale (than submeter) flow inhomogeneities, three different levels (low, moderate, and high) of the turbulent kinetic energy (TKE) input were considered—in the spirit of the direct numerical simulation (DNS) turbulence studies, which focus on accurate representation of the evolving flow but simplify initial and boundary conditions. In AGMS, for each TKE input, a control dry simulation was performed together with two moist simulations applying either bulk or detailed cloud microphysics.

The results presented in AGMS can be summarized as follows. As far as the evolution of enstrophy and TKE are concerned, the most significant impact of moist processes occurred at the low intensity of initial, large-scale (domain size) eddies (the TKE input is 2×10^{-4} m^2 s^{-2}, resulting in the maximum eddy dissipation rate of 5×10^{-4} m^2 s^{-3}). In this case, mixing and homogenization were dominated by the kinetic energy produced buoyantly due to droplet evaporation. Detailed microphysics, which explicitly accounts for the size dependence of the cloud droplet sedimentation and evaporation, appeared to have a comparatively small effect. The anisotropy between the horizontal and vertical, also observed in the laboratory (Banat and Malinowski 1999; Korczyk et al. 2006), prevailed even at the high intensity of initial large-scale eddies (the TKE input is 2×10^{-2} m^2 s^{-2}, the maximum eddy dissipation rate of 7×10^{-3} m^2 s^{-3}). Regardless of the TKE input, cloud droplet spectra at the end of the simulations (i.e., after homogenization) corresponded to neither the extremely inhomogeneous nor homogeneous mixing scenarios—the two asymptotic limits where, respectively, either the cloud droplet size or the number of cloud droplets remained constant. However, changing the TKE input from low to high shifted the mixing scenario toward the homogeneous case, corroborating the classical argument based on scale analysis (Baker and Latham 1979; Baker et al. 1980).

The relatively coarse spatial resolution of the AGMS simulations leaves uncertain the universality of the derived conclusions. The 0.01-m grid length is too coarse to resolve the molecular dissipation, whereupon a significant fraction of the total dissipation was provided by the model numerics. In effect, the calculations fell into the gray area between poorly resolved DNS and well-resolved implicit large-eddy simulation (LES; cf. Margolin et al. 2002, 2006; Domaradzki et al. 2003 for discussions). Such a coarse spatial resolution may also affect conclusions concerning microphysical transformations, because the edges of cloudy filaments are arguably less sharp when compared to mixing in natural and laboratory clouds (see Malinowski and Jaczewski 1999; Korczyk et al. 2006). Furthermore, the initial conditions in AGMS considered only half of the domain to be cloudy and half cloud free, thus providing no insights into the role the initial volume proportion of cloudy air played in the dynamics of mixing. The initial volume proportion of cloudy air is defined as $\chi \equiv V_c/(V_c + V_a)$, where V_c and V_a are, respectively, the initial volumes of the cloudy part and the clear air part of the computational domain. Here, χ controls the macroscopic properties of the buoyancy-reversing systems (see Grabowski 1993, and references therein) and constrains the microscopic transformations during mixing and homogenization. Furthermore, the initial size distribution of cloud droplets together with thermodynamic properties of cloudy and clear air also affect the transformations. It follows that the parameter space for the problem at hand is multidimensional, thus requiring a number of carefully planned numerical experiments to explore the sensitivities and draw general conclusions.

TABLE 1. A summary of the numerical simulations in the convergence study. The first column provides an acronym used in the reference to the set of simulations, the second column enumerates the simulations, the third column lists the grid resolution, the fourth identifies the microphysics scheme (B for bulk, D for detailed), the fifth specifies the input TKE (with L denoting low intensity), the sixth provides the initial cloud water mixing ratio within cloudy filaments, the seventh the initial relative humidity of clear air, and the eighth the initial volume proportion of the cloudy air χ.

Set of simulations	Simulation	Grid	Microphysics	TKE level	q_c (g kg^{-1})	RH (%)	χ
S1a	1	64^3	B	L	3.2	65	0.50
	2	128^3					
	3	256^3					
S1b	1	64^3	D	L	3.2	65	0.50
	2	128^3					
	3	256^3					

The next section summarizes the numerical model employed and provides essential information about the experimental setup, while referring the reader to AGMS for further details. Section 3 discusses the results of the convergence study—with DNS of the interfacial mixing in the limit—that seeks the optimal design of a large series of experiments with varying physical parameters. The principal result that coarse AGMS resolution has virtually no impact on the conclusions regarding microphysical transformations permits a wide sensitivity study, discussed in sections 4 and 5. Section 4 presents the results with varying χ using the same thermodynamic properties of cloudy and clear air as in AGMS, whereas the investigation of sensitivities to other parameters (e.g., liquid water mixing ratio, relative humidity, and microphysical characteristics) is included in section 5. A broader cloud physics context for model results is discussed in section 6, together with a comparison between model results and aircraft observations of microphysical properties of diluted cloudy volumes. A summary in section 7 concludes the paper.

2. Numerical model, modeling setup, and model simulations

The design of all experiments follows AGMS and augments Herring and Kerr's (1993) numerical study of dry transient decaying turbulence. The theoretical formulation, posited in AGMS, incorporates both bulk and detailed microphysics for the thermodynamics and a standard incompressible Boussinesq approximation for the dynamics. In the bulk microphysics, the cloud water mixing ratio is the sole variable representing cloud condensate, cloud condensate is carried by the flow, and cloudy volume is always saturated; that is, the adjustment (to saturation) is instantaneous. In contrast, in the detailed microphysics, 16 classes of radii represent the spectrum of cloud droplets in the range of 2.5–12 μm, each class is subject to a different sedimentation velocity, and condensation–evaporation takes a finite amount of time depending on local supersaturation; see AGMS for further details.

The computational domain of 0.64^3 m^3 is fixed in all simulations. The initial velocity field is constructed from a few lowest-wavenumber Fourier modes to mimic the instantaneous large-scale input of the TKE. The amplitudes selected to simulate three different large-scale inputs of TKE are 1.45×10^{-1}, 5.8×10^{-3}, and 1.62×10^{-4} m^2 s^{-2}—corresponding to high-, moderate-, and low-intensity levels of TKE input. Note that the span of the initial TKE is greater than that in AGMS (the corresponding values were 2.16×10^{-2}, 5.4×10^{-3}, and 2.16×10^{-4} m^2 s^{-2}) with the main difference being the significantly larger initial TKE for the high turbulence intensity regime. Similarly to AGMS, the resulting magnitude of the initial velocity fluctuations is in the range of a few centimeters per second (for the low-TKE input) to a few tens of centimeters per second (for the high-TKE input); for an illustration, see Fig. 1 in section 3 of AGMS. Initial conditions for the thermodynamic variables prescribe χ within the low-wavenumber filaments congruent with the velocity field. Here, χ is allowed to vary, whereas in all AGMS calculations it was fixed at 0.5.

To facilitate the presentation and analysis of over 50 numerical experiments, all simulations are divided into three groups termed convergence, reference, and sensitivity studies (convergence and reference studies are summarized in Tables 1 and 2; sensitivity studies are listed in Tables 3 and 4). Each group is subdivided into sets, each containing a number of experiments with a single variable parameter. In the convergence and reference studies, the initial air temperature is set to 293 K everywhere, the water vapor mixing ratio outside the cloudy filaments is 9.9 g kg^{-1} [relative humidity (RH) is 65%], and the initial cloud water within the filaments is 3.2 g kg^{-1}. These conditions are selected to mimic the laboratory investigations of cloud–clear air interfacial

TABLE 2. As in Table 1 but for the reference set of model simulations that investigates the sensitivity to the input TKE and the initial volume proportion of the cloudy air χ. An L, M, or H in the TKE column denotes low, moderate, or high intensity of the input TKE.

Set of simulations	Simulation	Grid	Microphysics	TKE level	q_c (g kg^{-1})	RH (%)	χ
S2a	1	64^3	D	L	3.2	65	0.13
	2						0.33
	3						0.43
	4						0.50
	5						0.67
	6						0.87
S2b	1	64^3	D	M	3.2	65	0.13
	2						0.33
	3						0.43
	4						0.50
	5						0.67
S2c	1	64^3	D	H	3.2	65	0.13
	2						0.33
	3						0.50
	4						0.87

mixing of Malinowski et al. (1998), Banat and Malinowski (1999), and Korczyk et al. (2006). In the sensitivity study, the initial cloud water mixing ratio, RH outside cloudy filaments, and selected microphysical parameters are systematically varied to bridge the gap between laboratory experiments and natural clouds. In all three studies the detailed microphysics simulations assume the initial cloud water distributed among three

TABLE 3. As in Table 1 but for a subset of sensitivity simulations that investigates the impact of the initial liquid water mixing ratio of cloudy filaments and the relative humidity of clear air.

Set of simulations	Simulation	Grid	Microphysics	TKE level	q_c (g kg^{-1})	RH (%)	χ
S3a	1	64^3	D	L	0.2	65	0.50
	2				0.5		
	3				1.0		
	4				1.5		
	5				3.2		
S4a	1	64^3	D	L	1.5	65	0.13
	2						0.33
	3						0.43
	4						0.50
	5						0.67
	6						0.87
S4b	1	64^3	D	L	0.5	65	0.13
	2						0.33
	3						0.43
	4						0.50
	5						0.67
	6						0.87
S4c	1	64^3	D	L	0.2	65	0.13
	2						0.33
	3						0.43
	4						0.50
	5						0.67
	6						0.87
S5a	1	64^3	D	L	3.2	30	0.50
	2					45	
	3					65	
	4					75	
	5					90	

TABLE 4. As in Table 1 but for a subset of sensitivity simulations that investigates the impact of microphysical characteristics of cloud droplets. The coefficient δ multiplies the standard terminal velocity of cloud droplets as given by Stokes's law. The coefficient γ multiplies the standard droplet evaporation rate $dr/dt = AS/r$ (S is supersaturation, r is droplet radius, $A = 10^{-10}$ m^2 s^{-1}).

Set of simulations	Simulation	Grid	Microphysics	TKE level	q_c (g kg^{-1})	RH (%)	χ	δ	γ
S6a	1	64^3	D	L	3.2	30	0.50	0	1
	2							1	
	3							2	
	4							4	
S6b	1	64^3	D	L	3.2	30	0.50	1	0.125
	2								0.25
	3								1.
	4								4.
	5								8.

classes of droplets with 25%, 50%, and 25% of the cloud water mixing ratio in the bins centered at 8, 8.75, and 9.5 μm, respectively. For completeness, the role of the initial cloud droplet size in the interfacial mixing is also investigated (see Table 4).

As in AGMS, simulations are performed until conditions close to the complete homogenization are achieved—for quantification, see AGMS, their Fig. 4 and the accompanying discussion—typically up to 25 s of real time. In low-TKE cases, the final conditions can evince small-scale inhomogeneities, such as the presence of trace cloud water in parts of the computational domain, despite that bulk mixing calls for the mean conditions to remain below saturation. Such instances will be presented.

All numerical procedures are the same as those used in AGMS. The new aspect of the present calculations is the removal of the mean (i.e., volume averaged) buoyancy at every time step of the model integration—equivalent to observing a Lagrangian parcel while neglecting the pressure variation due to vertical displacement (cf. section 2 in AGMS). As a result of droplet evaporation (and latent heat release), mean buoyancy is created; whereupon mean vertical velocity develops in the course of simulations. This mean velocity has no significance for the small-scale mixing and homogenization, because the turbulent stirring is driven by the small-scale vorticity dynamics where only the gradients of buoyancy, and not the mean, are relevant. In particular, removal of the mean buoyancy has no impact on the TKE and enstrophy; see the appendix for a discussion. Compared to the calculations of AGMS, the mean buoyancy removal improves the computational efficiency by relaxing the computational stability restrictions.

3. Convergence to DNS

The simulations in sets S1a and S1b of Table 1 investigate the convergence toward DNS and consist of calculations with increasing spatial (and temporal) resolution. The two sets use the bulk and detailed microphysics, respectively. Since droplet evaporation was shown in AGMS to have the strongest impact in simulations with low-TKE input, we select this most stringent scenario for the convergence study. The increase of the gridpoint number from 64^3 to 256^3 corresponds to the reduction of the grid length from 10^{-2} m to 0.25×10^{-2} m, the latter being comparable to the minimum Kolmogorov length scale in the low-TKE simulation (cf. Table 1 in AGMS).

Figure 1 compares the TKE evolutions in all simulations from sets S1a and S1b.[1] It shows that the TKE evolution is, to the first approximation, independent of the model resolution for both detailed and bulk microphysical models. For the detailed (bulk) model, the maximum value of about 2.2×10^{-3} (1.2×10^{-3} m^2 s^{-2}) is reached after 8–10 s into each simulation; the differences between bulk and detailed microphysics come from the absence of droplet sedimentation in the bulk model and its impact on the small-scale buoyancy (section 3 in Grabowski 1993). The important outcome is that the difference between the detailed and bulk model results depends marginally on the spatial resolution. A similar conclusion can be drawn from the time evolution of the mean temperature and moisture (not shown). In the detailed microphysics simulations, this also holds for the mean volume radius of cloud droplets $r_v \equiv \langle r^3 \rangle^{1/3}$, where $\langle\ \rangle \equiv (1/V) \int_V dv$ with V denoting the volume of the computational domain.

Figure 2 shows histories of the TKE dissipation rate for the detailed model simulations and the three grid resolutions (set S1b). In each panel, the dissipation is calculated in two different ways. First, the dissipation is estimated using the enstrophy representation, where

[1] Note that the respective Fig. 5 in AGMS that displays a TKE evolution at 64^3 gridpoint resolution employs the logarithmic scale.

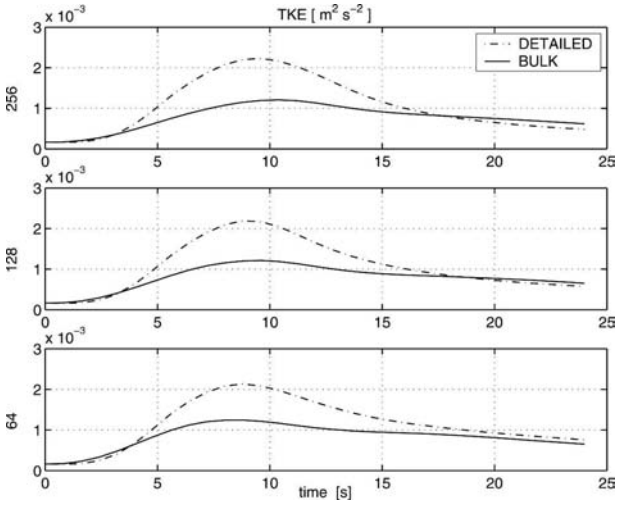

FIG. 1. Evolution of the TKE in simulations with the low-TKE input and with bulk (solid line) and detailed (dashed line) representations of the cloud microphysics: sets S1a and S1b. Results from simulations applying grid sizes of (top) 256^3, (middle) 128^3, and (bottom) 64^3.

the dissipation is equal to $2\nu\langle\Omega\rangle$ (see the appendix). Second, the dissipation is evaluated directly from the TKE evolution, while accounting for the domain-averaged buoyancy production $\langle w'B'\rangle$ [see Eq. (A.8)]. In the absence of any other dissipative processes (e.g., numerical diffusion), the two estimates of the TKE dissipation should match each other. Figure 2 documents that this is nearly the case for the 256^3 grid. For lower

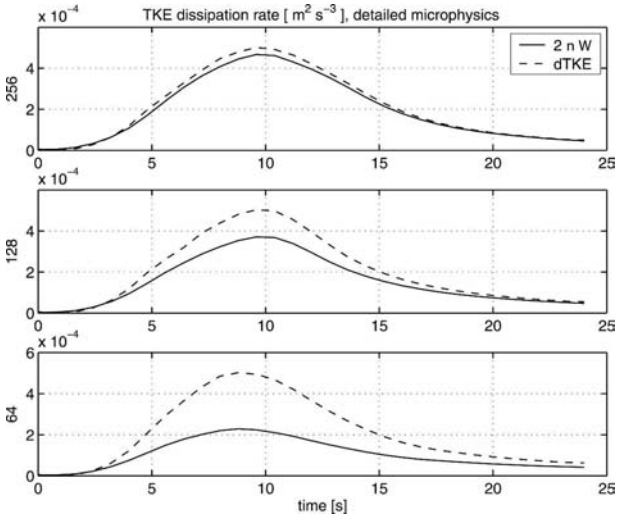

FIG. 2. Evolution of the TKE dissipation in the low-TKE input simulations applying detailed microphysics: set S1b. The solid lines are the theoretical predictions based on the enstrophy evolution, whereas the dashed line is the dissipation diagnosed from the TKE evolution and the buoyancy production term.

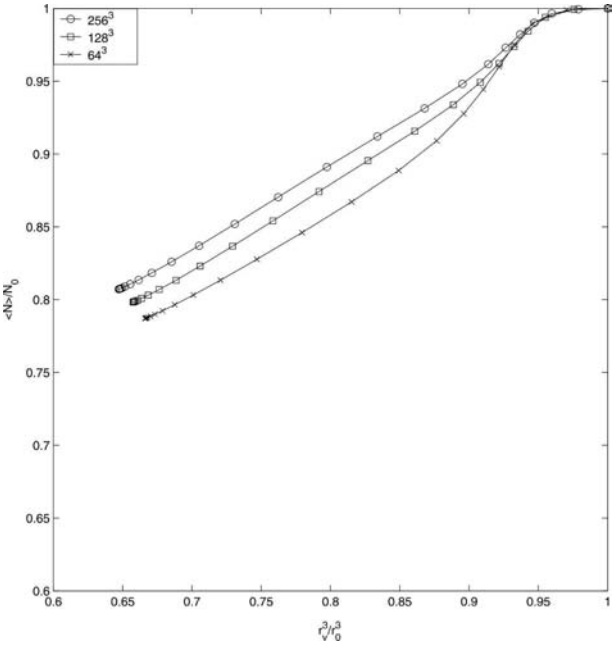

FIG. 3. Results from the detailed microphysics simulations with low-TKE input applying grid sizes of 256^3, 128^3, and 64^3 (set S1b) plotted in the $r - N$ diagram. The symbols along the lines are plotted every 0.8 s to demonstrate the elapsed time, from the starting point (upper-right corner) toward the lower left.

spatial resolutions, the effective numerical viscosity (Domaradzki et al. 2003; Margolin et al. 2006) supplements a significant fraction of the total TKE dissipation, while preserving the TKE evolution independent of the grid resolution (cf. Fig. 1). Clearly, the numerical viscosity provides an effective subgrid-scale model, resulting in the implicit LES at lower resolutions (Margolin et al. 1999, 2002).

Figure 3 shows the evolution of cloud droplets number, N, plotted as a function of the mean volume radius cubed, r_v^3, scaled by their initial values N_0 and r_{v0}, for the three simulations in set S1b. This diagram will be referred to as the $r - N$ diagram throughout the rest of this paper. It was adopted in AGMS after Brenguier and Burnet (1996); see also Chosson et al. (2004) and Burnet and Brenguier (2007, hereafter BB). In AGMS (their Fig. 13), only $(r_v/r_{v0})^3$ and N/N_0 of the final mixture were shown, whereas figures herein document the entire evolution of the microphysical parameters, from the start of the simulations [upper-right corner; (1, 1)] toward the completion of the mixing around (0.65, 0.80).

In the $r - N$ diagram, the final states of all possible microphysical realizations, for given initial conditions, reside on the hyperbola implied by $Nr_v^3 = \beta N_0 r_{v0}^3 =$ const (Fig. 13 in AGMS), where β, the ratio of the mean cloud water after and before the mixing, is given by the

FIG. 4. (right) Vertical cross section from the 256^3 detailed microphysics simulation with low-TKE input at t = 5 s and (left) a laser-sheet photograph of mixing structures observed in the laboratory. Both panels are about 0.6 m × 0.6 m. Direction of gravity is from top to bottom.

bulk thermodynamic properties of cloudy and cloud-free air and χ (cf. section 5 in AGMS for a discussion). The impacts of the two limiting conceptual models of the microscale homogenization on cloud droplet spectra are easily identified in the $r - N$ diagram. The homogeneous model assumes that all droplets are exposed to the same environmental conditions during homogenization. It follows that all droplets experience some evaporation and the number of cloud droplets does not change. Consequently, homogeneous mixing is represented by a horizontal line segment from (1, 1) to (β, 1). In the extremely inhomogeneous model (Baker and Latham 1979; Baker et al. 1980), on the other hand, some droplets evaporate completely whereas others do not change their sizes at all. In such a case, the number of droplets decreases, but their size remains constant. Such a change is represented by a vertical line segment from (1, 1) to (1, β).

Results shown in Fig. 3 document that the mixing in the three simulations falls somewhere in between the two limiting conceptual models, and that the simulated microphysical transformations only weakly depend on the model resolution. The latter finding corroborates the validity of the results reported in AGMS, and indicates the adequacy of the 64^3 grid for the sensitivity studies discussed in subsequent sections.

To illustrate the relevance of our numerical studies to the cloud chamber experiment of Malinowski et al. (1998) and Korczyk et al. (2006)—the original motivation behind this work—Fig. 4 compares a cross section from the 256^3 low-TKE input simulation with a laser-sheet photograph of cloudy and clear air filaments in the laboratory experiment. The size of the two-dimensional cross section is approximately the same (about 0.6 m × 0.6 m). The photograph from the cloud chamber shows finescale structures within cloudy filaments that result from the scattering of laser light by individual droplets. In contrast, the numerical model output displays only a continuous cloud water field. The resemblance of the larger-scale topological structures (filaments and eddies) between the numerical model result and laboratory experiment is noteworthy.

4. Microphysical transformations during turbulent mixing: Reference study

The simulations in sets S2a, S2b, and S2c of Table 2 investigate the sensitivity of microphysical transformations to the TKE input and initial volume proportion of the cloudy air χ. All three sets use the detailed microphysics, 64^3 grid, as well as fixed initial liquid water in cloudy filaments and the relative humidity of clear air.

All simulations in AGMS assumed an idealized mixing scenario with $\chi = 0.5$. Here, we consider a range of $\chi \in]0, 1[$. Varying χ has important implications for the thermodynamic state after homogenization. This is illustrated in Fig. 5, a mixing diagram for cloudy and clear air (cf. Grabowski 1993) with the thermodynamic initial conditions assumed. The diagram shows the density temperature T_ρ [see Emanuel 1994, Eq. (4.3.6)] after homogenization as a function of χ; $T_\rho \approx T(1 + \epsilon q_v - q_c)$, where T is the air temperature, $\epsilon + 1 \equiv R_v/R_d$ is the ratio of the gas constants for water vapor and dry air, and q_v and q_c are the water vapor and cloud water

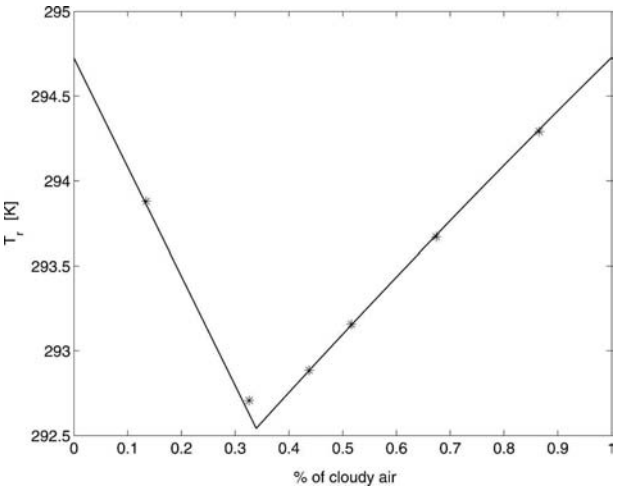

FIG. 5. Density temperature T_ρ after homogenization as a function of the initial proportion of the cloudy air volume χ for the reference group of model simulations (cf. Table 2). Solid lines represent theoretical predictions; the asterisks represent values calculated using final thermodynamic properties from numerical simulations with detailed microphysics and the low-TKE input (i.e., set S2a).

mixing ratios. The mixing diagram consists of two line segments (theoretical predictions) whose common point ($\chi \approx 0.34$, $T_\rho \approx 292.6$ K) represents a state where the homogenized mixture is at saturation and contains no cloud water. This is the mixture with the lowest density temperature, that is, with the smallest buoyancy gT'_ρ/T_{ρ_o} (here, g is the gravitational acceleration and the prime denotes deviations from the initial value T_{ρ_o} of the clear air, the same as in the cloudy air in the reference setup). The segment to the left of the common point ($\chi < 0.34$) corresponds to the unsaturated, cloud-free homogenized mixtures, whereas the segment to the right ($\chi > 0.34$) corresponds to the saturated cloudy mixtures. The asterisks on the segments show T_ρ of the homogenized mixture, as simulated by the model, for selected values of χ, applying detailed microphysics and low-TKE input.

The mixing diagram documents that the model accurately reproduces the bulk thermodynamic properties of the homogenized mixture.[2] Furthermore, the mixing diagram shows that varying χ results in substantial changes to T_ρ. The estimated negative buoyancy after the homogenization ranges from about -1.7×10^{-2} m s^{-2} for $\chi = 0.87$ to about -7.7×10^{-2} m s^{-2} $\chi = 0.33$.

[2] The case $\chi = 0.33$ has still not reached the equilibrium conditions. Traces of cloud water are present in the computational domain at the end of this simulation because the final point in the $r - N$ diagram is not at (0, 0); see Fig. 6.

The impact of these T_ρ variations on the mean buoyancy, and vertical velocity, has already been explained in the closing paragraph of section 2 (and the appendix). The impact on the microphysical transformations is discussed below.

The results from simulation sets S2a, S2b, and S2c are summarized in Figs. 6, 7, and 8, respectively, for the low-, medium-, and high-TKE inputs. The figures show the evolution of the domain-average TKE, enstrophy, temperature, and the mean volume radius $r_v \equiv \langle r^3 \rangle^{1/3}$. Furthermore, the evolution of the cloud droplets number N and the mean volume radius cubed r_v^3 are combined in the $r - N$ diagram.

For the low-TKE input (Fig. 6) most of the TKE is generated as a result of the evaporation of cloud droplets during the first 10 s of the simulation. The evolutions of the mean temperature and the mean volume radius are consistent with our expectations following the basic physics of mixing: the lowest temperature is obtained for $\chi = 0.33$ (cf. Fig. 5) and the mean radius of the homogenized mixture decreases with diminishing χ. For simulations with different χ, the maximum values of TKE are in the range from about 2×10^{-3} to about 3×10^{-3} m^2 s^{-2}, whereas the maximum values of the mean enstrophy are from about 4 to about 8 s^{-2}. These differences are relatively small considering the differences in the realizable negative buoyancy (within a factor of 5; cf. Fig. 5). Moreover, the actual value of the maximum TKE (around $t = 10$ s) is unrelated to the potential for buoyancy reversal. For instance, the largest and smallest TKE maxima are reached in simulations with, respectively, $\chi = 0.13$ and $\chi = 0.87$—the two cases with the lowest potential for the buoyancy reversal. The lack of correlation between TKE and the potential for the buoyancy reversal suggests that the interfacial mixing occurs locally, as a result of molecular diffusion and droplet sedimentation across the interface, while χ, a global measure, is of secondary importance. In other words, the global mixing proportion affects the mean buoyancy—hence, the Lagrangian parcel's acceleration and mean vertical velocity, see the appendix—and not the dynamics of the small-scale turbulent mixing.

The most intriguing aspect is the evolution of microphysical properties displayed in the $r - N$ diagram. All mixing events appear to follow the same path, starting from the upper-right corner of the diagram and proceeding toward the lower-left corner. This implies that the average microphysical properties are approximately the same regardless of the progress of mixing. For instance, the transient microphysical properties for $\chi = 0.13$, 0.33, and 0.43 all pass close to the final properties

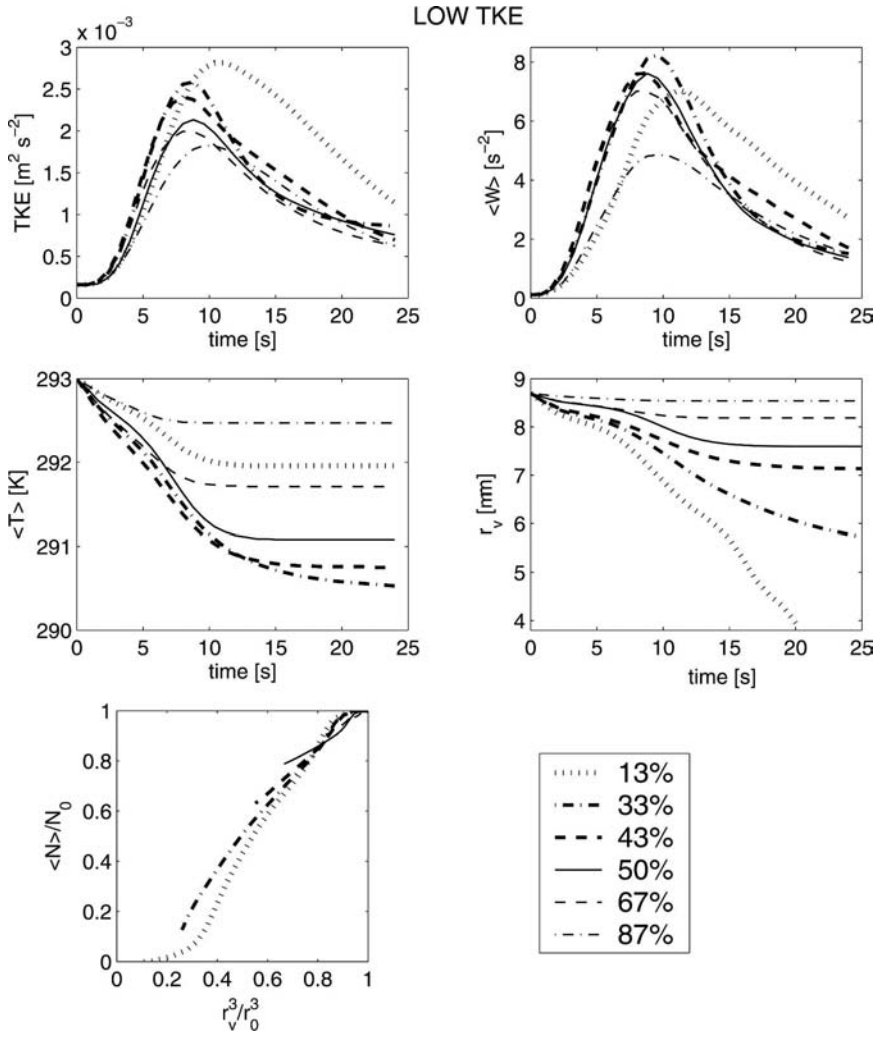

FIG. 6. Results from the set of numerical simulations with low-TKE input and detailed microphysics applying the reference setup: set S2a. The evolution of the (top left) TKE and (top right) mean enstrophy. The evolution of the (middle left) mean temperature and (middle right) mean volume radius. (bottom left) The evolution of the microphysical properties using the $r - N$ diagram.

of the mixing event with $\chi = 0.50$. In the vicinity of this point (in the diagram) in all transient states, the mean cloud water equals the final value for the mixing event with $\chi = 0.50$. This is an important finding because it implies that the mean microphysical properties, as measured by the mean number of droplets and the mean volume radius, only weakly depend on the progress of mixing. This suggests that it may be possible to design a relatively simple parameterization to describe microphysical transformations during entrainment and mixing, without the need to consider whether microscale homogenization is already completed or not.

The overall similarities of the TKE and microphysical evolutions observed in the S2a calculations for the low-TKE input are reproduced in the S2b and S2c simulations with moderate- (Fig. 7) and high- (Fig. 8) TKE inputs, respectively. The paths of the TKE evolutions are predetermined by the input velocity perturbations. The differences in the individual evolutions of the TKE and enstrophy, for different χ, are relatively minor, diminish with increasing TKE input, and vanish in the high-TKE input case. Furthermore, although the $r - N$ diagrams show, consistent with the low-TKE input case, that microphysical properties depend only weakly on the progress of the mixing, there are systematic differences between the three sets of simulations. In particular, a higher-TKE input leads to mixing that is initially more of the homogeneous type (i.e., the lines

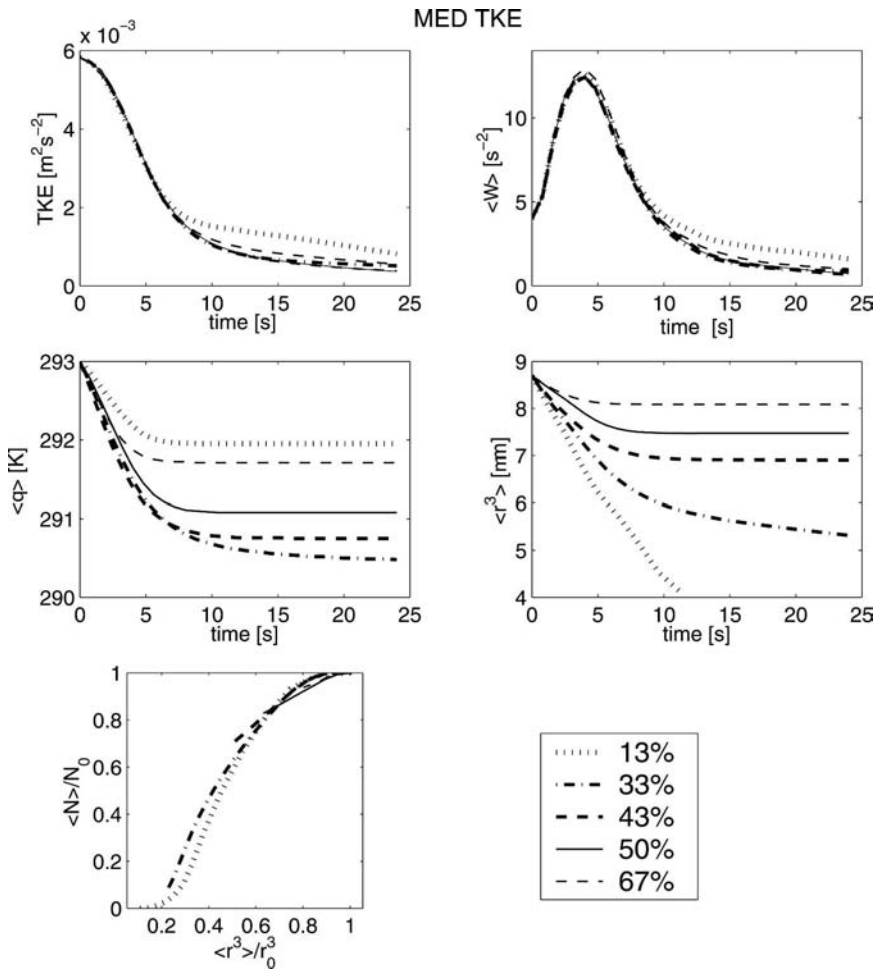

FIG. 7. As in Fig. 6 but for simulations with moderate-TKE input from set S2b.

tend to be horizontal) and changes toward the extremely inhomogeneous mixing at later stages (i.e., the lines are not far from vertical).

5. Microphysical transformations during turbulent mixing: Sensitivity study

The simulations described in the previous section apply a selected set of thermodynamic and microphysical parameters, representative of conditions in the laboratory experiments (Malinowski et al. 1998; Banat and Malinowski 1999; Korczyk et al. 2006). Here, additional simulations are performed to shed light on the universality of the derived conclusions. The sensitivity simulations fall into two distinct categories. The first investigates the impact of bulk thermodynamic properties, such as the liquid water mixing ratio of cloudy filaments, the global mixing proportion χ, and the initial relative humidity (RH) of the dry air. These simulations form sets S3a, S4a, S4b, S4c, and S5a (cf. Table 3). The second group investigates the impact of the initial spectrum of cloud droplets on the resulting microphysical transformations. These simulations are grouped into two sets, S6a and S6b, detailed in Table 4.

a. Impact of initial bulk thermodynamic properties

In the first set of simulations, S3a, the initial liquid water within the cloudy filaments is systematically varied, from 0.2 to 3.2 g kg^{-1}. The amount of liquid water in the cloudy filaments changes the bulk mixing diagram shown previously in Fig. 5. In general, decreasing the liquid water mixing ratio increases the mixing proportion χ that corresponds to the saturated mixture (i.e., the intersection of the two line segments in Fig. 5) and increases the minimum buoyancy. The mixing proportions corresponding to the saturated mixtures are $\chi = 0.34$, 0.52, 0.77, and 0.88 for cloud water equal to, respectively, 3.2, 1.5, 0.5, and 0.2 g kg^{-1}. The minimum

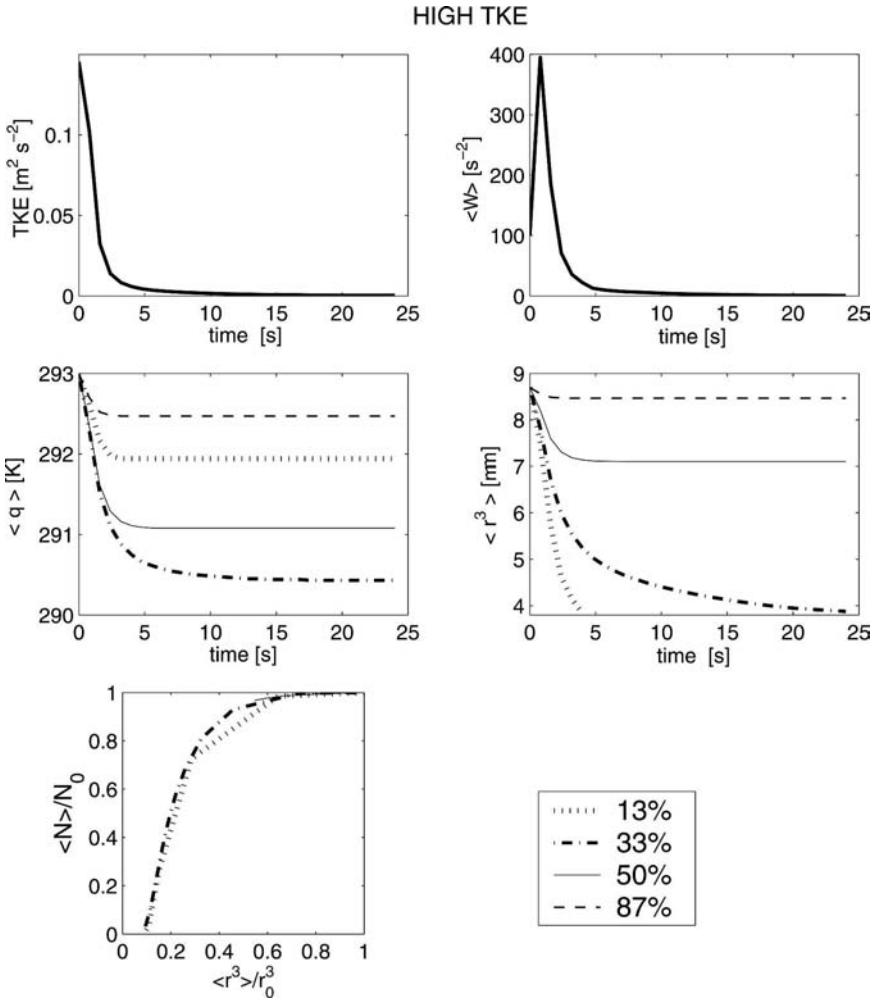

FIG. 8. As in Fig. 6 but for simulations with high-TKE input from set S2c.

buoyancies are -7.7×10^{-2}, -4.5×10^{-2}, and -0.6×10^{-2} m s^{-2} for cloud water equal to, respectively, 3.2, 1.5, and 0.5 g kg^{-1}. There is no buoyancy reversal for a cloud water mixing ratio of 0.2 g kg^{-1} because the saturated mixture is positively buoyant, with a buoyancy of 1.4×10^{-2} m s^{-2}, which is about half of the buoyancy of the cloudy air. The assumed range of the initial liquid water aims at representing conditions ranging from cumulus (the high end of the liquid water) to stratocumulus (the low end).

Figure 9 documents the results of simulations with thermodynamic properties as in simulations described in the previous section and $\chi = 0.5$, but with systematically varied liquid water within cloudy filaments, from 0.2 to 3.2 g kg^{-1} (set S3a). Because $\chi = 0.5$, only the highest initial liquid water mixing ratio (3.2 g kg^{-1}) leads to the homogenized mixture with some condensate; all other cases result in subsaturated mixtures without any liquid water.[3] As Fig. 9 shows, in agreement with results discussed in the preceding section, the resulting maximum TKE varies within a factor of 2 between all simulations, and the evolution on the $r - N$ diagram follows a similar path to the results shown in Fig. 6 (i.e., close to the lower left-upper right diagonal of the diagram).

The next three figures document the impact of varying mixing proportions χ on mixing characteristics with various initial liquid water mixing ratios within the cloudy filaments; see sets S4a, S4b, and S4c in Table 3. Except for the initial liquid water, the simulations are otherwise identical to those shown in Fig. 6. Figures 10,

[3] The case with a 1.5 g kg^{-1} initial cloud water mixing ratio results in a mixture practically at saturation; note that this simulation has still not reached the equilibrium conditions because the final point in the $r - N$ diagram is not at (0, 0).

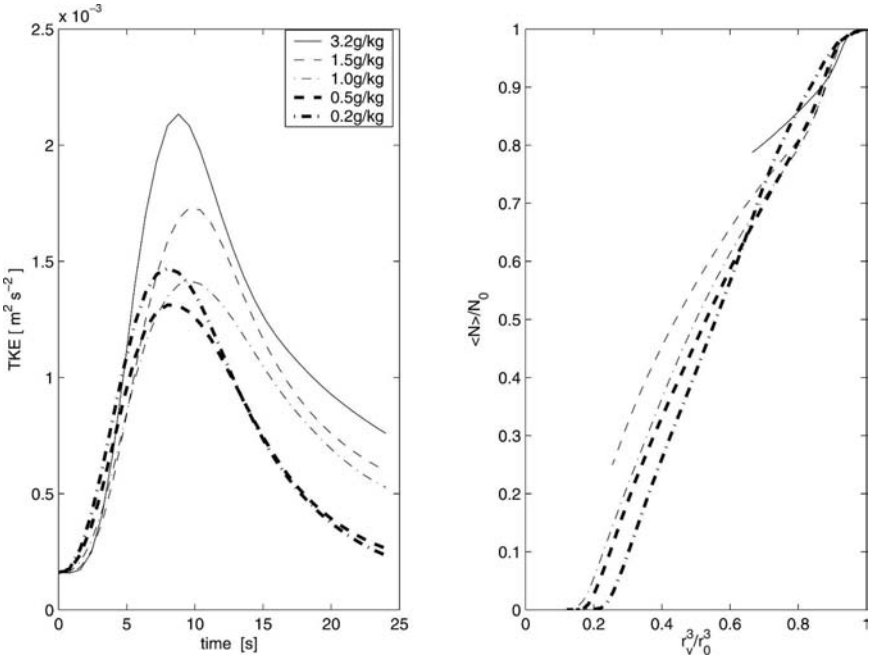

FIG. 9. Results from the set of numerical simulations with low TKE, detailed microphysics, $\chi = 0.5$, and systematically varied cloud water mixing ratio within cloudy filaments: set S3a. The evolutions of the (left) TKE and (right) $r - N$ diagram.

11, and 12 document the results from simulations with initial liquid water mixing ratios of 1.5, 0.5, and 0.2 g kg^{-1}, respectively. As discussed above, reducing the initial liquid water within cloudy filaments reduces the potential for buoyancy reversal and consequently leads to a systematic decrease of the TKE levels in simulations with decreasing initial cloud water. Similar to the reference study simulations, the maximum TKE for a

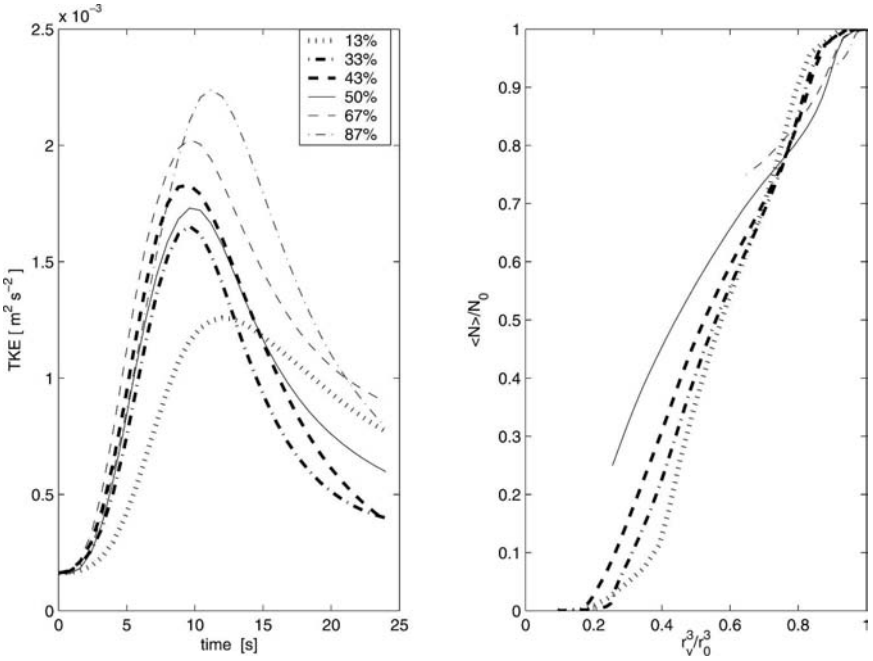

FIG. 10. Results from the set of numerical simulations with low TKE, detailed microphysics, cloud water mixing ratio within cloudy filaments of 1.5 g kg^{-1}, and systematically varied global mixing proportion χ: set S4a. The evolutions of the (left) TKE and (right) $r - N$ diagram.

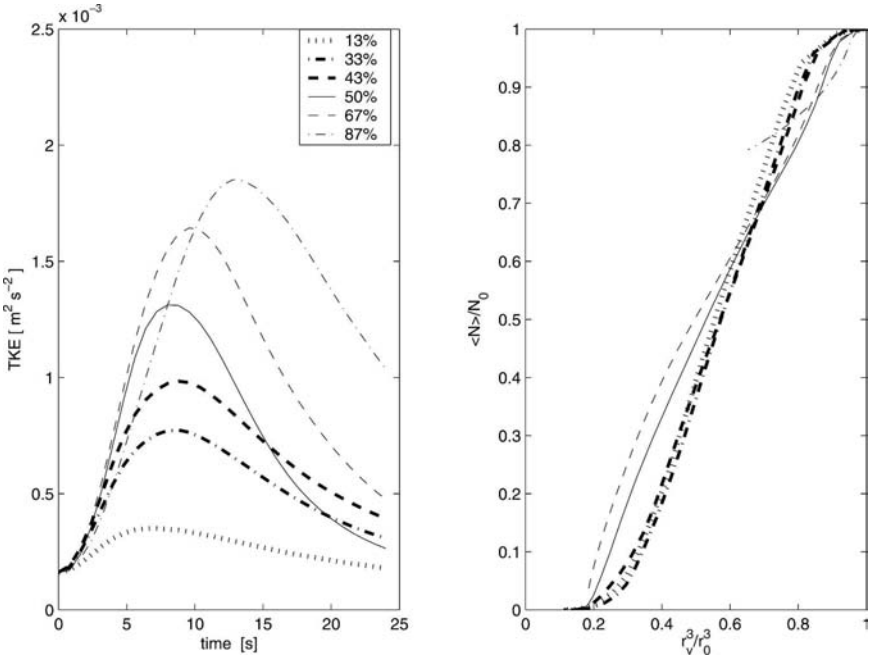

FIG. 11. As in Fig. 10 but for cloud water mixing ratio within cloudy filaments of 0.5 g kg^{-1}: set S4b.

given initial liquid water mixing ratio appears uncorrelated with the global mixing proportion $\mathcal{X}$. Again, as in previous cases with the low-TKE input, the results follow a similar path in the $r - N$ diagram, from the upper right toward the lower left.

The last set of simulations investigating the impact of thermodynamic properties considers systematic changes of the RH within clear air filaments, with the cloud water of cloudy filaments equal to 3.2 g kg^{-1}, low input TKE, and the global mixing proportion $\mathcal{X} = 0.5$

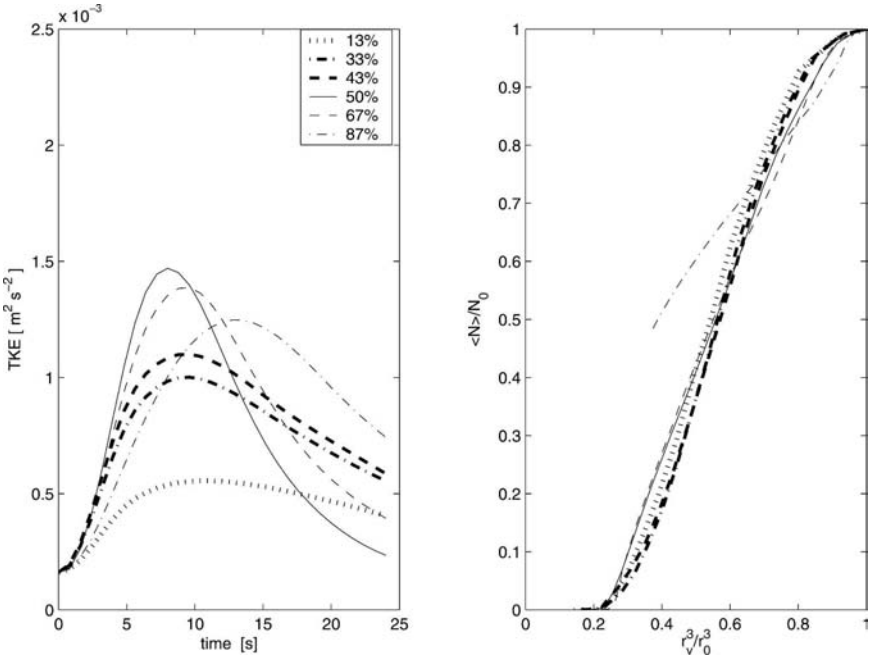

FIG. 12. As in Fig. 10 but for cloud water mixing ratio within cloudy filaments of 0.2 g kg^{-1}: set S4c.

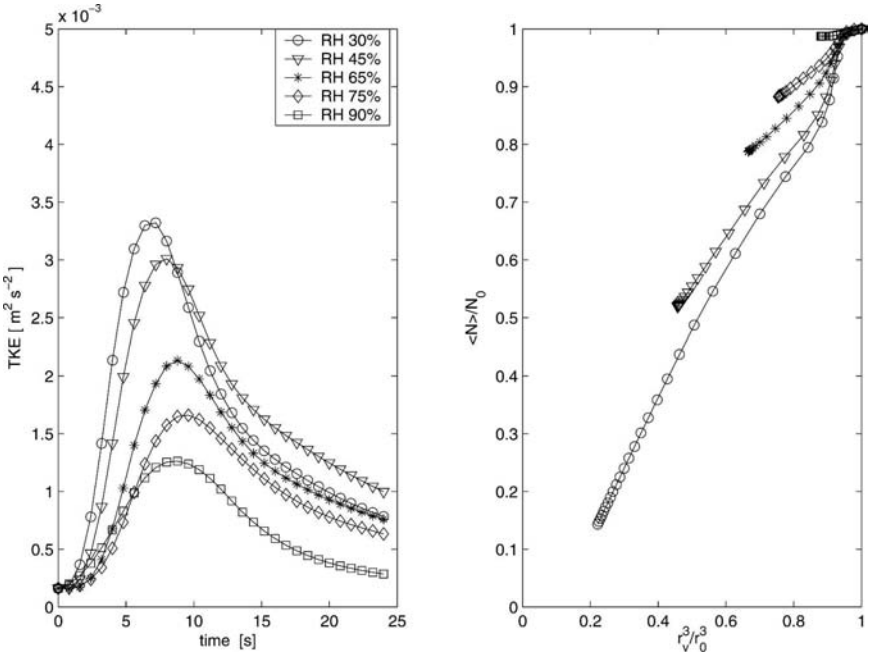

FIG. 13. Results from the set of numerical simulations with low TKE, detailed microphysics, cloud water mixing ratio within cloudy filaments of 3.2 g kg^{-1}, $\chi = 0.5$, and systematically varied relative humidity within clear air filaments: set S5a. The evolutions of the (left) TKE and (right) $r - N$ diagram. The symbols along the lines are plotted every 1.6 s to demonstrate the elapsed time.

(set S5a in Table 3). The range of RH considered in this set is from 30% to 90%. The mixing diagrams for these conditions are characterized by shifting the mixing proportion corresponding to the minimum buoyancy from $\chi = 0.52$ for RH = 30% to $\chi = 0.13$ for RH = 90%. It follows that for the assumed mixing proportion $\chi = 0.5$, all but the RH = 30% simulation lead to saturated cloudy mixtures after homogenization. However, since the RH = 30% simulation has not reached the equilibrium conditions, the final point in the $r - N$ diagram is not at (0, 0). The resulting liquid water mixing ratio ranges from about 0.4 g kg^{-1} for RH = 45% to about 1.5 g kg^{-1} for RH = 90%.

The results of simulations with variable RH are summarized in Fig. 13. The RH of clear air filaments has two distinct effects. First, RH affects the amount of cloud water that has to evaporate during homogenization as discussed above. This impacts both the amount of liquid water left at the end of simulations and the negative buoyancy generated during mixing. The decreasing amount of liquid water with the decreasing RH is demonstrated by the length of the mixing lines in the $r - N$ diagram for the fixed global mixing proportion of 0.5 (note that the RH = 30% simulation is terminated before the equilibrium conditions are reached). Changes of the negative buoyancy, on the other hand, affect the maximum TKE generated during mixing. The maximum TKE monotonically increases with decreasing RH, with the TKE for RH of 30% approximately three times higher than for RH of 90%. Second, the RH affects the rate of evaporation of cloud droplets that fall across the cloud–clear air interface into the subsaturated air. As a result, the RH of clear air filaments impacts the homogeneity of mixing, with high RH implying more homogeneous mixing because the homogeneous mixing is anticipated when droplet evaporation time is much longer than the time of turbulent homogenization (Baker and Latham 1979; Baker et al. 1980).[4] This is evident in the $r - N$ diagram shown in Fig. 13, which documents that it is no longer true that mixing histories are close to the diagonal of the $r - N$ diagram, especially for high RH of clear filaments. However, the departures from the diagonal are relatively minor compared to the scatter of curves in Figs. 6–12, especially for lower values of RH.

[4] It has to be pointed out, however, that the distinction between the homogeneous and extremely inhomogeneous mixing vanishes once the relative humidity of clear air is 100% because no droplet evaporation is needed.

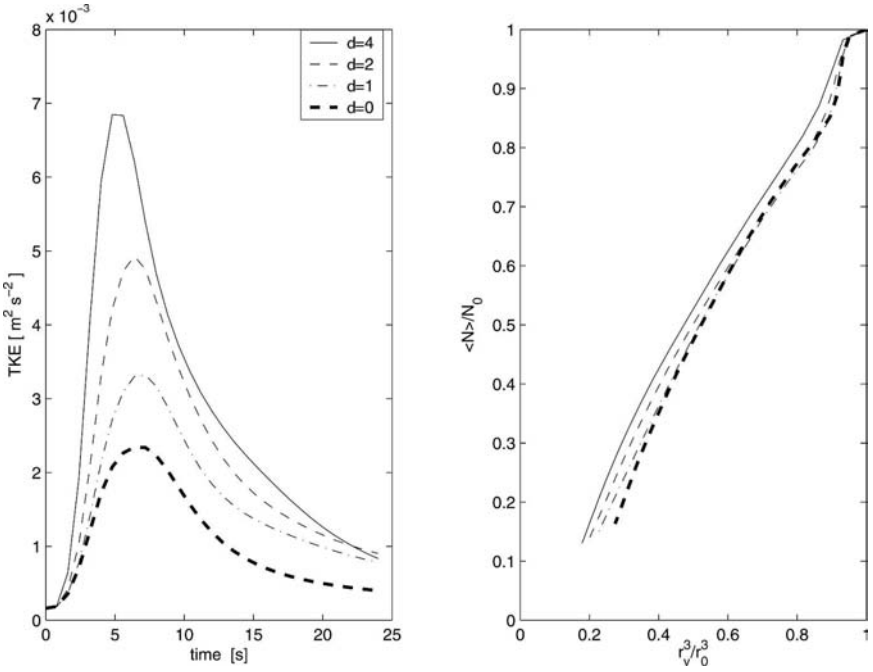

FIG. 14. Results from the set of numerical simulations with low TKE, detailed microphysics, cloud water mixing ratio within cloudy filaments of 3.2 g kg^{-1}, RH within clear air filaments of 30%, $\mathcal{X} = 0.5$, and systematically varied sedimentation rate of cloud droplets: set S6a. The evolutions of the (left) TKE and (right) $r - N$ diagram.

b. *Impact of initial cloud microphysical properties*

The final two sets of model simulations, S6a and S6b in Table 4, investigate the impact of the initial cloud droplet spectrum on the microphysical transformations. In general, the initial spectrum of cloud droplets is anticipated to play a role via two separate mechanisms. First, larger cloud droplets fall faster across the cloud–clear air interface and may result in a different evolution of the TKE and different spectral changes during homogenization. Second, larger cloud droplets require more time to evaporate (for the same ambient conditions) and, thus, can shift the mixing scenario toward more homogeneous mixing. It follows that increasing the droplet size for the same TKE input and the same properties of the clear air should result in more homogeneous mixing. To show that such elementary considerations do provide useful insights, the final two sets of model simulations are performed (S6a and S6b) in the setup corresponding to the low-TKE input, 3.2 g kg^{-1} of cloud water within initial cloudy filaments, RH of cloud-free filaments of 30%, and $\mathcal{X} = 0.5$.

To focus the investigation (of the impact of the initial cloud droplet spectrum on the microphysical transformations), we adopt an idealized approach, where the initial spectrum of cloud droplets remains fixed, but the sedimentation rate of droplets and their evaporation rate, both depending on the droplet size, are varied separately. Technically, this is achieved by including factors δ and γ (constant for each simulation) in the formulas for droplet terminal velocity and droplet evaporation rate, respectively. For instance, by assuming that the sedimentation rate v_t is four times the original value (given by Stokes's law) and the evaporation rate dr/dt is half of the original value (for the same ambient conditions), the results mimic conditions with two times larger initial cloud droplets. The advantage of such an approach is that it emphasizes relevant physical mechanisms through which the initial droplet spectrum affects the mixing and homogenization.

Figure 14 shows results from set S6a of simulations where droplet terminal velocity is multiplied by a factor varying from 0 (i.e., no sedimentation) to 4. Arguably, such a spread covers the expected range of droplet sizes in natural clouds. As the figure shows, increasing the sedimentation rate increases the maximum TKE during mixing. This is consistent with the expectation that more rapid transport of cloud droplets across the cloud–clear air interface should result in enhanced negative buoyancy, and consequently more buoyantly produced TKE. The impact on the microphysical transformations, on the other hand, is rather small as documented by the $r - N$ diagram.

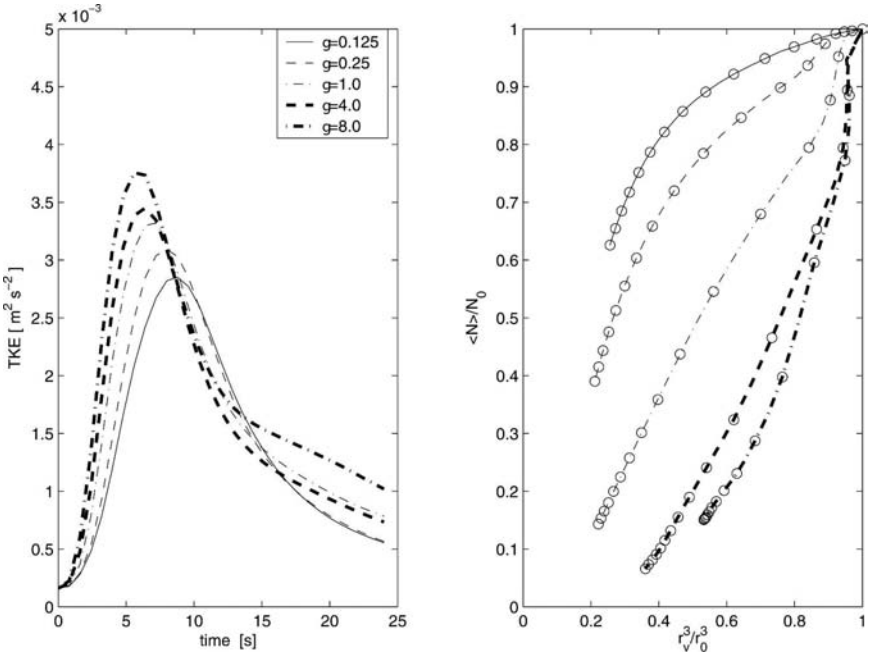

FIG. 15. As in Fig. 14 but with systematically varied evaporation rate of cloud droplets: set S6b. The circles along the lines in the $r - N$ diagram represent the elapsed time, with each circle plotted every 1.6 s.

In contrast, the rate of droplet evaporation affects mostly microphysical transformations. This is documented in Fig. 15, which shows the results of a series of simulations from set S6b, where the droplet growth rate dr/dt is multiplied by a factor (constant in each simulation) ranging from 0.125 to 8. Such a range exceeds the range of droplet sizes anticipated in natural clouds because it corresponds to droplets with radii 8 times larger and 8 times smaller than in the standard setup. In fact, considering that the initial cloud droplet spectrum in the reference setup has continental characteristics (i.e., the mean droplet radius is around 9 μm), model results related to natural clouds would fall within the limits given by the simulations with the factors of 0.25 and 1. As Fig. 15 documents, the impact of such changes on the TKE is rather small (especially when compared to the impact through the terminal velocity), but the character of the mixing is significantly affected. In agreement with the discussion toward the end of the previous section (i.e., the impact of clear air RH), larger droplets (i.e., droplets with longer evaporation time) result in mixing that is initially more homogeneous (i.e., the trajectory in the $r - N$ diagram lies above the diagonal). Smaller droplets, on the other hand, featuring shorter evaporation time, lead to initially more inhomogeneous mixing.

In summary, as far as the microphysical transformations during entrainment and mixing are concerned, the initial cloud droplet spectrum seems to mostly affect the rate of droplet evaporation (i.e., larger droplets requiring more time to evaporate), whereas droplet sedimentation mostly affects TKE generated during mixing, with higher TKE present in simulations with larger droplets. These results imply that, in otherwise identical situations, larger cloud droplets lead to a more homogeneous mixing through the combination of their ability to generate more TKE via enhanced sedimentation and their longer lifetime.

6. Discussion

For decades, entrainment and mixing have been postulated as crucial processes affecting the spectrum of cloud droplets (cf. Lasher-Trapp et al. 2005; BB, and references therein). The homogeneous and extremely inhomogeneous mixing models represent two limits of admissible microphysical transformations during a mixing event with prescribed bulk properties of the two air parcels. As illustrated by results discussed in AGMS and in this paper, the final state of the homogenized mixture has microphysical properties somewhere between the two limiting cases, with both the number of droplets and the mean droplet size modified. Since typically a considerable fraction of the volume of a cumulus or stratocumulus cloud is diluted by entrainment (e.g., Blyth 1993; Wang and Albrecht 1994; Moeng 2000),

microphysical transformations during small-scale turbulent mixing are important for warm rain development (e.g., Lasher-Trapp et al. 2005) and radiative transfer through the cloudy atmosphere (Chosson et al. 2004; Grabowski 2006).

Lasher-Trapp et al. (2005) investigated the impact of entrainment on the broadening of cloud droplet spectra, and the role of varying supersaturation histories during parcel ascent toward the observation point (Cooper 1989). Their results corroborate the concept of the entrainment leading to the development of a secondary mode, in addition to the mode produced by the adiabatic ascent from the cloud base (cf. Paluch and Knight 1984; Brenguier and Grabowski 1993). The relative magnitudes of the two modes, however, appeared to be sensitive to the assumed mixing scenario—homogeneous versus extremely inhomogeneous—with realistic droplet spectra produced in simulations blending the two limits.

Chosson et al. (2004) documented the impact of the mixing assumption on the radiative transfer by performing LESs of a stratoculumulus cloud and applying the results to a radiation transfer model. Because the radiation model requires cloud droplet size distribution, information that is unavailable from the bulk model, the following approach was used. In undiluted (adiabatic) cloud volumes, droplet size distributions were calculated using an adiabatic growth model and the observed droplet spectrum near the cloud base. In the diluted volumes, on the other hand, the homogeneous and extremely inhomogeneous mixing scenarios were separately considered and the sensitivity to these two extreme limits was investigated. The results turned out to be surprisingly sensitive to the assumed mixing scenario, with the cloud optical depth about 35% larger for the homogeneous mixing than for the extremely inhomogeneous mixing scenario. This was argued to have far-reaching consequences for satellite remote sensing of clouds.

A similar investigation for the case of cumulus convection was reported in Grabowski (2006). Therein, it was shown that varying the assumptions concerning the homogeneity of mixing in diluted volumes of convective clouds had a major impact on the amount of solar energy reaching the surface. In particular, the first indirect effect of atmospheric aerosols, the so-called Twomey effect (Twomey 1974, 1977), turned out to be the same in either clean clouds assuming the homogeneous mixing or polluted clouds with the extremely inhomogeneous mixing.

To assess meteorological implications of our results, we attempt to relate model results to cloud observations. The $r - N$ diagram adopted throughout this paper uses the total number of droplets involved in the mixing event as one of the variables—a natural choice in reductionistic model simulations. However, it can be easily converted into the Brenguier and Burnet (1996) diagram that uses measured droplet concentration; see also Chosson et al. (2004) and BB. This is demonstrated in Fig. 16, where the $r - N$ diagram shown in Fig. 6 is transformed such that the vertical axis is the concentration C, that is, the number of droplets N divided by the volume of the computational domain (the $r - C$ diagram). Because the adiabatic concentration C_o corresponds to the situation where the entire computational domain is filled with the initial cloudy air, the starting points for lines representing simulations with different mixing proportions $\mathcal{X}$ are no longer at the upper-right corner, that is, at (1, 1). Instead, the starting point for each simulation in the $r - C$ diagram represents the initial mixing proportion; that is, it is located at (1, $\mathcal{X}$). Moreover, because the total number of droplets does not change during homogeneous mixing (unless all droplets evaporate), paths that correspond to the homogeneous mixing are horizontal lines connecting the starting point (1, $\mathcal{X}$) with the nondimensional mean volume radius determined by the bulk mixing characteristics (i.e., the cloud water left after homogenization). Clearly, representing the mixing in the $r - C$ diagram obscures the similarity of solutions obtained with various mixing proportions in the $r - N$ diagram.

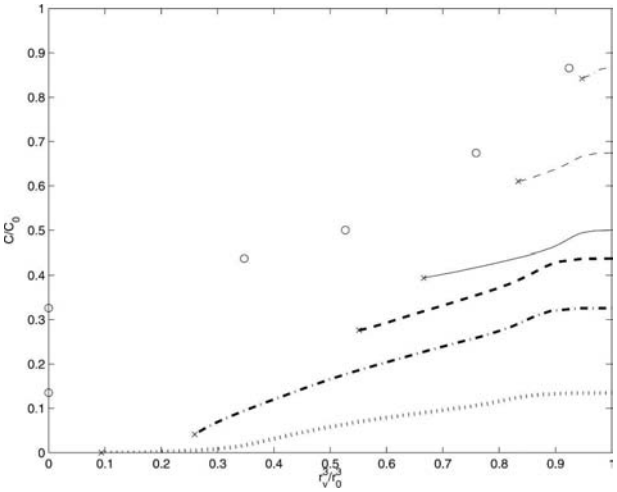

FIG. 16. The $r - C$ diagram from the set of simulations shown in Fig. 6. The circles show the ending points of the horizontal trajectories, which represent homogeneous mixing given the initial mixing proportion $\mathcal{X} = C/C_o$.

Converting aircraft observations to the format of the $r - N$ diagram is not an easy task. First, the limitations of the aircraft instrumentation need to be recognized.

The entrainment and mixing between a cloud and its clear environment are often envisioned as a two-stage process, where the initial stirring produces filaments of cloudy and clear air, and molecular mixing across the interface separating the filaments completes the microscale homogenization (e.g., Broadwell and Breidenthal 1982; Jensen and Baker 1989; Malinowski and Zawadzki 1993). When analyzing data from an aircraft flying through a volume still in the first stage of mixing, results obtained with instruments not capable of resolving microscale structures can easily be interpreted as representing extremely inhomogeneous mixing (see a discussion in section 5 of Paluch and Baumgardner 1989). This purely instrumental effect results in an apparent dilution of cloud droplets, as illustrated by the starting points of the trajectories in the $r - C$ diagram in Fig. 16. Moreover, a "mixing event," where a given mass of cloudy air initiates and completes mixing with a given mass of clear air, is difficult to observe in natural clouds.

One can attempt, nevertheless, to convert aircraft observations into the $r - N$ diagram applying the following strategy. First, one has to assume that cloud dilution observed at a given level results from a single mixing event between undiluted cloudy air at this level and subsaturated environmental air at the same level. This assumption is likely often violated in clouds because of a possibility of multiple mixing events and of the vertical displacement of a parcel undergoing mixing. It does, however, allow for a straightforward conversion of cloud observations into the $r - N$ diagram. The procedure is to first use the observed total water (the sum of the water vapor and cloud water mixing ratios, which is invariant when there is no precipitation) to derive the mixing proportion between the undiluted cloudy air and subsaturated environmental air at the same level. Multiplying the mixing proportion by the undiluted droplet concentration (estimated from the area of the cloud that is as close to adiabatic as possible) gives an estimate of the number of droplets (per unit volume) involved in the mixing event. This number, together with the mean volume radius of the undiluted cloudy air, are then used to normalize the observed local concentration and the local mean volume radius. The result of such a procedure for the Fast-Forward Scattering Spectrometer Probe (Fast-FSSP) data (Burnet and Brenguier 2002; BB) collected during one of the Météo-France Merlin IV flights during the Small Cumulus Microphysics Experiment (July–August 1995, in Florida) is shown in Fig. 17. The result is a large cluster of points corresponding to neither the homogeneous nor the extremely inhomogeneous mixing scenarios, which is consistent with our DNS study.

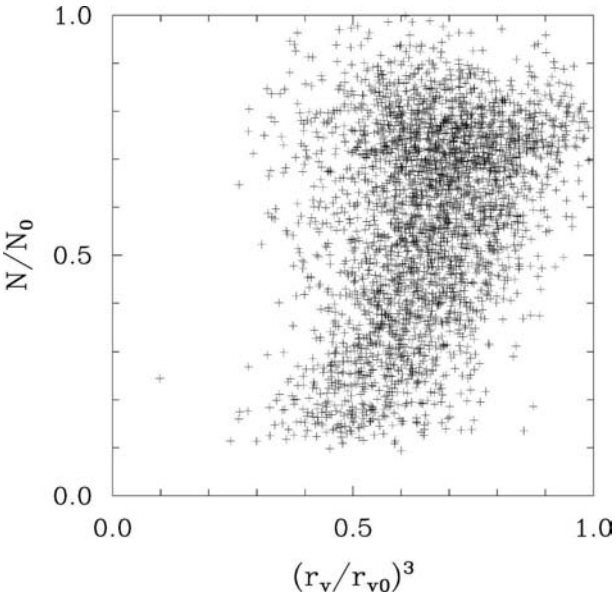

FIG. 17. The $r - N$ diagram for cloud penetrations near the top of cumulus clusters at an altitude of about 2400 m during the 5 August flight of the Météo-France Merlin IV (from 1402:30 to 1514:00 UTC) during the Small Cumulus Microphysics (SCMS) experiment. Each point corresponds to observed cloud droplet properties converted to the number of droplets involved in a single mixing event.

Arguably, the most significant conclusion of our study is that the average microphysical properties of the mixture only weakly depend on the macroscopic mixing proportion and on the progress of mixing. This implies that a parameterization can be developed for representing the small-scale inhomogeneities and their impact on microphysical characteristics. Such a parameterization would be a DNS-derived microphysical subgrid-scale model for a dynamical LES that assumes grid-scale homogenized-dependent variables. Furthermore, the reduced parameterization would be equally relevant to models with bulk microphysics, when needed to supply microphysical parameters for radiative transfer (e.g., Chosson et al. 2004; Grabowski 2006). Our results suggest that it is feasible to account for departures from the homogeneity of subgrid-scale mixing in contemporary cloud models. Possible approaches will be the subject of future research.

Although our results do have potentially significant implications for the warm rain development and radiative transfer through warm (ice free) clouds, it is premature to speculate on the specifics. This is because of the small volume considered in the simulations compared to the mean free path of a photon inside a cloud (typically several tens of meters or longer) and the lack of vertical motion of the parcel during mixing and ho-

mogenization, which may provide fresh nucleation and/or "superadiabatic" growth of some droplets. These issues will be addressed in future studies where a subgrid-scale parameterization developed using the current results is applied in LES simulations of warm clouds. Work in this area has already begun and modeling results will be reported upon as they become available.

7. Summary

The reported computational study of decaying moist turbulence extends the calculations of AGMS. Inspired by laboratory experiments (Malinowski et al. 1998; Korczyk et al. 2006), the adopted modeling setup follows the DNS of dry transient isotropic homogeneous turbulence (Herring and Kerr 1993), in an attempt to bridge the gap between laboratory experiments and natural clouds. The emphasis is on the final stage of the entrainment and mixing, when the filamentation by large-scale eddies is already completed and mixing/evaporative cooling takes place (Jensen and Baker 1989). The present work examines the accuracy of the AGMS results obtained at relatively coarse spatial resolution and the sensitivity of solutions to the initial thermodynamic properties of cloudy and clear air, mixing proportions, and microphysical properties of cloud droplets.

The first issue is resolved by means of a convergence study for the fixed initial conditions and physical domain. The analysis of a series of simulations with 64^3, 128^3, and 256^3 grid points demonstrates that at the highest resolution ($\Delta x = 0.25 \times 10^{-2}$ m) calculations resolve the molecular dissipation, that is, fall into the DNS regime. The DNS experiments accurately represent physical processes from $O(1\text{ m})$ down to the Kolmogorov scale. Most importantly, the integral characteristics of the DNS results match the results of coarser-grid simulations, both here and in AGMS, including turbulence evolution as well as the turbulence effect on cloud microphysics. The implications of this finding are twofold. First, this corroborates earlier results (Domaradzki et al. 2003; Margolin et al. 1999, 2002, 2006; and references therein) on implicit LESs of *dry* turbulence with a subgrid-scale model supplied by effective numerical viscosity. Second, it enables extensive parametric studies of cloud–clear air mixing at affordable resolutions.

Several sets of detailed microphysics simulations are performed at the low spatial resolution. First, the role of the initial volume proportion χ in turbulent mixing and homogenization is investigated using low-, moderate-, and high-TKE inputs and thermodynamic parameters as in AGMS. The parameter χ strongly impacts the buoyancy of the homogenized volume (Fig. 5), but its effect on the turbulence appears small. This is true even for the low-TKE input, where most of the TKE is produced buoyantly, stemming from droplet evaporation near the cloud–clear air interface. This result shows that local buoyancy reversal and microscale dynamics are independent of the global mixing proportion. In contrast, the mean vertical velocity is forced by the mean buoyancy, via (A4), and thus depends on χ.

The set of detailed microphysics simulations with variable χ and variable input TKE demonstrates that the evolution of microphysical properties in the $r - N$ diagram (adapted from Brenguier and Burnet 1996) follows a universal path that depends primarily on the initial TKE input. For the low-TKE input, the path of microphysical transformations is along the diagonal in the $r - N$ diagram, reflecting equal changes of the dimensionless droplet number and the mean volume radius cubed during the homogenization. For higher-input TKE, the mixing is more complicated. In early stages, mixing shifts toward the homogeneous mixing, corroborating the classical argument based on scale analysis (Baker and Latham 1979; Baker et al. 1980; Jensen and Baker 1989). At later stages, when most of the TKE is already dissipated, the mixing resembles the extremely inhomogeneous type. The similarity of the mixing evolution in the $r - N$ diagram (i.e., the lack of dependence on χ) paves the way to subgrid-scale microphysics models that account for cloud dilution due to entrainment.

In subsequent sensitivity simulations using the low-TKE input, the impact of thermodynamic and microphysical properties of cloudy and clear air on mixing characteristics is studied. The initial cloud water within cloudy filaments has a small impact, with microphysical transformations for low-TKE input again close to the diagonal in the $r - N$ diagram. The relative humidity (RH) of clear air filaments turns out to be more important, with higher RH resulting in a more homogeneous mixing and microphysical transformations deviating from the diagonal in the $r - N$ diagram. This is consistent with the fact that high RH increases droplet evaporation time. An additional shift toward the homogeneous mixing can be provided by assuming larger cloud droplets, featuring longer evaporation time and allowing for more TKE generation.

Finally, there are processes neglected in the present study that may play a role in natural clouds. First, the dynamics of cloud droplet motion is simplified by neglecting droplet inertia, a resultant of gravity and drag. According to the calculations of Bajer et al. (2000),

Vaillancourt et al. (2002), and Falkovich and Pumir (2004), the inertial effects can influence the local concentration of cloud droplets even in a homogeneous cloud. Although the quantitative estimates are uncertain (see Grabowski and Vaillancourt 1999 for a discussion), recent experimental results show fluctuations of the local concentration of droplets of the order of a few percent (Jaczewski and Malinowski 2005), which are most likely insignificant for the processes investigated herein. Second, for the problem at hand, a continuous model for representing the discrete cloud water phase becomes questionable at the DNS resolution $\Delta x = 2.5 \times 10^{-3}$ m, which is already on the order of the mean distance between cloud droplets $O(10^{-3}$ m). An alternative multiphase system approach that accounts for individual droplet dynamics and evaporation (Vaillancourt et al. 2002) might be considered in future studies to address such outstanding issues. Finally, fresh nucleation of cloud droplets due to entrainment has no impact on the spectrum of cloud droplets in the current simulations. In reality, however, fresh nucleation is anticipated (cf. Paluch and Knight 1984; Brenguier and Grabowski 1993; Su et al. 1998; Lasher-Trapp et al. 2005). Our interpretation of previous results is that fresh nucleation happens when a cloudy parcel undergoing mixing with its subsaturated environment continues to rise. This effect, neglected in the current study, should be investigated in the future as well. One possibility is to use the same modeling setup, but allowing for a gradual change of the ambient pressure as the mixing and homogenization progresses. This may bring some parts of the computational domain to saturation and allow nucleation of new cloud droplets. All of the above factors warrant further numerical studies.

Acknowledgments. This work was supported by the European Commission Fifth Framework Program's Project EVK2-CT2002-80010-CESSAR, by NCAR's Clouds in Climate and Geophysical Turbulence Programs, by the Department of Energy's (DOE) Climate Change Prediction Program (CCPP), by Los Alamos National Laboratory's Directed Research and Development Project "Resolving the Aerosol Climate Water Puzzle (20050014DR)," and by NOAA Grant NA05OAR4310107. The computations were performed at the Interdisciplinary Center for Mathematical and Computational Modeling of Warsaw University and at NCAR. Comments on earlier versions of this manuscript by Jean-Louis Brenguier, Steve Krueger, and Raymond Shaw are gratefully acknowledged. We thank Jean-Louis Brenguier and Fred Burnet for providing us the aircraft data used in Fig. 17. NCAR is sponsored by the National Science Foundation.

APPENDIX

Mean Buoyancy Removal

The momentum and mass continuity equations for the incompressible Boussinesq fluid can be written compactly as follows:

$$\frac{\partial \mathbf{v}}{\partial t} + \mathbf{v} \cdot \nabla \mathbf{v} = -\nabla \pi + \mathrm{k}B + \nu \nabla^2 \mathbf{v}, \tag{A1}$$

$$\nabla \cdot \mathbf{v} = 0, \tag{A2}$$

where $\mathbf{v} = (u, v, w)$ is the velocity vector, π is the pressure perturbation normalized by the reference density, $\mathbf{k} = (0, 0, 1)$ is the unit vector in the vertical, B denotes the buoyancy, and ν is the kinematic viscosity. With periodic boundary conditions and the generation of domain-averaged buoyancy (due to the evaporation of cloud droplets), the mean vertical velocity develops during the course of the simulations. In particular, integrating (A2) over the fixed horizontal domain, applying periodic boundary conditions in the horizontal, and dividing by the integration surface area results in

$$\frac{\partial \overline{w}}{\partial z} = 0, \tag{A3}$$

thereby implying a uniform (in the vertical) horizontally averaged vertical velocity $\overline{w}$ equal to the volume-averaged $\langle w \rangle$.

Integrating the flux form of (A1) over the entire volume of the domain, applying triply periodic boundary conditions, and dividing by the volume reduces (A1) to the equation governing the volume-averaged velocity:

$$\frac{d}{dt} \langle \mathbf{v} \rangle(t) = \mathbf{k} \langle B \rangle(t). \tag{A4}$$

Equation (A4) states that the volume-averaged horizontal velocities remain constant in time, whereas the volume-averaged vertical velocity responds to the evolution of the volume-averaged buoyancy.

Decomposing the velocity and buoyancy fields into time-dependent volume-averaged components and perturbations

$$\mathbf{v} = \langle \mathbf{v} \rangle + \mathbf{v}', \quad B = \langle B \rangle + B', \tag{A5}$$

and inserting (A5) into (A1), while using (A4), results in the equivalent, perturbation form of (A1):

$$\frac{\partial \mathbf{v}'}{\partial t} + \mathbf{v}' \cdot \nabla \mathbf{v}' = -\nabla \pi + \mathbf{k}B' + \nu \nabla^2 \mathbf{v}' - \langle \mathbf{v} \rangle \cdot \nabla \mathbf{v}'. \tag{A6}$$

The last term on the rhs of (A6) represents the advection of the perturbation velocity by the mean velocity $\langle \mathbf{v} \rangle$. With triply periodic boundary conditions, it has no contribution to the enstrophy $\Omega \equiv \frac{1}{2}\langle(\nabla \times \mathbf{v}')^2\rangle$ and the turbulent kinetic energy $\mathrm{TKE} \equiv \frac{1}{2}\langle \mathbf{v}'^2 \rangle$. This is because $\langle \langle \mathbf{v} \rangle \cdot \nabla \mathbf{v}' \rangle \equiv 0$ as well as $\nabla \times (\langle \mathbf{v} \rangle \cdot \nabla \mathbf{v}') = \langle \mathbf{v} \rangle \cdot \nabla(\nabla \times \mathbf{v}')$, thereby implying $\langle \langle \mathbf{v} \rangle \cdot \nabla \Omega \rangle \equiv 0$. Consequently, the evolution equations for the volume-averaged enstrophy and TKE do not depend on the last term on the rhs of (A6). In particular,

$$\frac{d\mathrm{TKE}}{dt} = \langle w'B' \rangle + \nu \langle \mathbf{v}' \nabla^2 \mathbf{v}' \rangle, \tag{A7}$$

or, using the relation $\langle \mathbf{v}' \nabla^2 \mathbf{v}' \rangle \equiv -2\langle \Omega \rangle$ (Frisch 1995),

$$\frac{d\mathrm{TKE}}{dt} = \langle w'B' \rangle - 2\nu \langle \Omega \rangle. \tag{A8}$$

For the sake of computational efficiency, the mean buoyancy accumulated over the time step is subtracted at the end of each time step—a "mean buoyancy removal" procedure. Mathematically, this is equivalent to integrating (A1) with B replaced by B', or integrating (A6) without the last term on the rhs. According to (A4), the mean buoyancy removal assures $\langle \mathbf{v} \rangle \equiv 0$. As shown above, this has no impact on the domain-averaged turbulence characteristics.

REFERENCES

Andrejczuk, M., W. W. Grabowski, S. P. Malinowski, and P. K. Smolarkiewicz, 2004: Numerical simulation of cloud–clear air interfacial mixing. *J. Atmos. Sci.,* **61,** 1726–1739.

Bajer, K., K. M. Markowicz, and S. P. Malinowski, 2000: Influence of the small-scale turbulence structure on the concentration of cloud droplets. *Proc. 13th Int. Conf. on Clouds and Precipitation,* Reno, NV, International Commission on Clouds and Precipitation, 159–162.

Baker, M. B., and J. Latham, 1979: The evolution of droplet spectra and the rate of production of embryonic raindrops in small cumulus clouds. *J. Atmos. Sci.,* **36,** 1612–1615.

——, R. G. Corbin, and J. Latham, 1980: The influence of entrainment on the evolution of cloud droplet spectra: I. A model of inhomogeneous mixing. *Quart. J. Roy. Meteor. Soc.,* **106,** 581–598.

Banat, P., and S. P. Malinowski, 1999: Properties of the turbulent cloud–clear air interface observed in the laboratory experiment. *Phys. Chem. Earth,* **24B,** 741–745.

Blyth, A. M., 1993: Entrainment in cumulus clouds. *J. Appl. Meteor.,* **32,** 626–640.

Brenguier, J.-L., and W. W. Grabowski, 1993: Cumulus entrainment and cloud droplet spectra: A numerical model within a two-dimensional dynamical framework. *J. Atmos. Sci.,* **50,** 120–136.

——, and F. Burnet, 1996: Experimental study of the effect of mixing on droplet spectra. *Proc. 12th Int. Conf. on Clouds and Precipitation,* Zurich, Switzerland, International Commission on Clouds and Precipitation, 67–70.

Broadwell, J. E., and R. E. Breidenthal, 1982: A simple model of mixing and chemical reaction in turbulent shear layer. *J. Fluid Mech.,* **125,** 397–410.

Burnet, F., and J. L. Brenguier, 2002: Comparison between standard and modified forward scattering spectrometer probes during the Small Cumulus Microphysics Study. *J. Atmos. Oceanic Technol.,* **19,** 1516–1531.

——, and ——, 2007: Observational study of the entrainment-mixing process in warm convective clouds. *J. Atmos. Sci.,* in press.

Chosson, F., J.-L. Brenguier, and M. Schröder, 2004: Radiative impact of mixing processes in boundary layer clouds. *Proc. Int. Conf. on Clouds and Precipitation,* Bologna, Italy, International Commission on Clouds and Precipitation, 371–374.

Cooper, W. A., 1989: Effects of variable droplet growth histories on droplet size distributions. Part I: Theory. *J. Atmos. Sci.,* **46,** 1301–1311.

Domaradzki, J. A., Z. Xiao, and P. K. Smolarkiewicz, 2003: Effective eddy viscosities in implicit modeling of turbulent flows. *Phys. Fluids,* **15,** 3890–3893.

Emanuel, K. A., 1994: *Atmospheric Convection.* Oxford University Press, 580 pp.

Falkovich, G., and A. Pumir, 2004: Intermittent distributions of heavy particles in a turbulent flow. *Phys. Fluids,* **16,** L47–L50, doi:10.1063/1.1755722.

Frisch, U., 1995: *Turbulence: The Legacy of A. N. Kolmogorov.* Cambridge University Press, 310 pp.

Grabowski, W. W., 1993: Cumulus entrainment, fine scale mixing and buoyancy reversal. *Quart. J. Roy. Meteor. Soc.,* **119,** 935–956.

——, 2006: Indirect impact of atmospheric aerosols in idealized simulations of convective–radiative quasi-equilibrium. *J. Climate,* **19,** 4664–4682.

——, and P. Vaillancourt, 1999: Comments on "Preferential concentration of cloud droplets by turbulence: Effects on the early evolution of cumulus cloud droplet spectra." *J. Atmos. Sci.,* **56,** 1433–1436.

Herring, J. R., and R. M. Kerr, 1993: Development of enstrophy and spectra in numerical turbulence. *Phys. Fluids,* **5A,** 2792–2798.

Jaczewski, A., and S. P. Malinowski, 2005: Spatial distribution of cloud droplets investigated in a turbulent cloud chamber. *Quart. J. Roy. Meteor. Soc.,* **131,** 2047–2062.

Jensen, J. B., and M. B. Baker, 1989: A simple model for droplet spectral evolution during turbulent mixing. *J. Atmos. Sci.,* **46,** 2812–2829.

Korczyk, P. M., S. P. Malinowski, and T. A. Kowalewski, 2006: Mixing of cloud and clear air in centimeter scales observed in laboratory by means of particle image velocimetry. *Atmos. Res.,* in press.

Lasher-Trapp, S. G., W. A. Cooper, and A. M. Blyth, 2005: Broadening of droplet size distributions from entrainment and mixing in a cumulus cloud. *Quart. J. Roy. Meteor. Soc.,* **131,** 195–220.

Malinowski, S. P., and I. Zawadzki, 1993: On the surface of clouds spectral evolution during turbulent mixing. *J. Atmos. Sci.,* **50,** 5–13.

——, and A. Jaczewski, 1999: Laboratory investigation of the droplet concentration at the cloud–clear air interface. *Phys. Chem. Earth,* **24B,** 477–480.

——, I. Zawadzki, and P. Banat, 1998: Laboratory observations of cloud clear air mixing in small scales. *J. Atmos. Oceanic Technol.,* **15,** 1060–1065.

Margolin, L. G., P. K. Smolarkiewicz, and Z. Sorbjan, 1999:

Large-eddy simulations of convective boundary layers using nonoscillatory differencing. *Physica D,* **133,** 390–397.

——, ——, and A. A. Wyszogrodzki, 2002: Implicit turbulence modeling. *J. Fluid Eng.,* **124,** 862–867.

——, ——, and ——, 2006: Dissipation in implicit turbulence models: A computational study. *ASME J. Appl Mech.,* **73,** 469–473.

Moeng, C.-H., 2000: Entrainment rate, cloud fraction, and liquid water path of PBL stratocumulus clouds. *J. Atmos. Sci.,* **57,** 3627–3643.

Paluch, I. R., and C. A. Knight, 1984: Mixing and the evolution of cloud droplet size spectra in a vigorous continental cumulus. *J. Atmos. Sci.,* **41,** 1801–1815.

——, and D. G. Baumgardner, 1989: Entrainment and fine-scale mixing in a continental convective cloud. *J. Atmos. Sci.,* **46,** 261–278.

Su, C.-W., S. K. Krueger, P. A. McMurtry, and P. H. Austin, 1998: Linear eddy modeling of droplet spectral evolution during entrainment and mixing in cumulus clouds. *Atmos. Res.,* **47–48,** 41–58.

Twomey, S., 1974: Pollution and the planetary albedo. *Atmos. Environ.,* **8,** 1251–1256.

——, 1977: The influence of pollution on the shortwave albedo of clouds. *J. Atmos. Sci.,* **34,** 1149–1152.

Vaillancourt, P. A., M. K. Yau, P. Bartello, and W. W. Grabowski, 2002: Microscopic approach to cloud droplet growth by condensation. Part II: Turbulence, clustering, and condensational growth. *J. Atmos. Sci.,* **59,** 3421–3435.

Wang, Q., and B. A. Albrecht, 1994: Observations of cloud-top entrainment in marine stratocumulus clouds. *J. Atmos. Sci.,* **51,** 1530–1547.